JGR Space Physics

RESEARCH ARTICLE
10.1029/2026JA035112

Resolving GLE 77 of November 11, 2025: First Simultaneous Recovery of Neutron and Muon Energy Spectra

A. Chilingarian[1], B. Sargsyan[1], L. Kozliner[1], and T. Karapetyan[1]

[1]A.I.Alikanyan National Lab (Yerevan Physics Institute), Yerevan, Armenia

Key Points:

- Simultaneous neutron and muon energy spectra of Ground Level Enhancement (GLE) 77 were obtained at Aragats using the Aragats Solar Neutron Telescope and SEVAN
- Comparison with the CORSIKA + GEANT4 reconstruction chain indicates a relatively soft, cutoff-limited GLE77 event
- The proposed GLE analysis scheme can be applied for space weather alerting

Correspondence to:
A. Chilingarian,
chili@aragats.am

Citation:
Chilingarian, A., Sargsyan, B., Kozliner, L., & Karapetyan, T. (2026). Resolving GLE 77 of November 11, 2025: First simultaneous recovery of neutron and muon energy spectra. *Journal of Geophysical Research: Space Physics*, *131*, e2026JA035112. https://doi.org/10.1029/2026JA035112

Received 20 JAN 2026
Accepted 24 MAY 2026

Author Contributions:
Conceptualization: A. Chilingarian
Data curation: T. Karapetyan
Formal analysis: A. Chilingarian
Investigation: B. Sargsyan, L. Kozliner
Software: B. Sargsyan
Validation: L. Kozliner, T. Karapetyan
Visualization: B. Sargsyan
Writing – original draft: A. Chilingarian
Writing – review & editing: A. Chilingarian

Abstract Ground Level Enhancements (GLEs) are rare solar energetic particle events in which relativistic solar protons produce measurable increases in secondary neutrons and muons at the ground level. For space weather operations, the key real-time measurement is the spectral hardness of the solar proton population. This indicates that the SEP protons extend far enough to include substantial fluxes above 50 MeV, posing risks to satellite electronics, electrical lines, and pipelines on Earth. We analyze GLE 77 (11 November 2025) using measurements from Aragats (3,200 m) at the Aragats Solar Neutron Telescope (ASNT) and the SEVAN Light spectrometric detector. We employ energy-deposit histograms of simultaneously detected muon- and neutron-enriched fluxes to recover differential energy spectra and derive the muon-to-neutron ratio. The spectra are compared with a unified forward-modeling chain (CORSIKA atmospheric cascades and GEANT4 detector response) processed through the same reconstruction procedure as the data. Both instruments reveal a two-peak temporal structure that coincides with neutron monitor observations. The observations are most consistent with a dominant contribution from primary protons near 9–10 GeV, that is, near and slightly above the local geomagnetic cutoff. These neutron–muon spectrometric diagnostics offer a practical method for near-real-time tracking of proton spectral hardness during future GLEs.

Plain Language Summary Sometimes, solar eruptions accelerate protons to such high energies that they create additional secondary particles in Earth's atmosphere, which can then be detected on the ground. These rare events are called ground-level enhancements. In this study, we analyze GLE 77 from 11 November 2025, using two detectors located together at Aragats in Armenia. We obtained muon- and neutron-enriched energy spectra and compared the muon-dominated component with atmospheric cascade simulations. The observations are best explained if most solar protons were near the local geomagnetic cutoff, with an effective upper energy around 9–10 GeV. This suggests that GLE 77 was much softer than the most intense historical ground-level events. The method developed here shows that local neutron–muon spectrometry can help determine the actual hardness of a solar proton event.

1. Introduction

Ground Level Enhancements (GLEs) are high-energy events in which solar protons reach energies high enough to produce secondary cascades detectable by ground-based detectors (Shea & Smart, 2012). GLEs are the highest-energy form of solar energetic protons (SEP; Reames, 2013); 77 officially recorded GLEs have mostly been linked to major eruptive flares and CME-driven shocks (Butikofer & Fluckiger, 2015). GLE 77 on 11 November 2025, one of the strongest events of the neutron-monitor era (although its high-energy component appears to be much softer than that of GLE 69), offers an exceptional chance to test such methods with modern ground-based and space-borne observations.

Energy spectra of muons and neutrons produced by solar proton interactions in the atmosphere serve as direct indicators of the solar proton population and the acceleration environment in flare regions (Reames, 2021). Their overall production spectrum index closely relates to the energy distribution of shock- or reconnection-accelerated ions. Therefore, precisely characterizing the spectral shapes offers rare insights into time-dependent acceleration processes on the Sun.

In space weather and solar physics, the key real-time parameter is the spectral index of the solar proton spectrum during an event. This spectral index influences (a) the flux of the highest-energy solar particles, (b) radiation hazards at aviation altitudes and in near-Earth space, and (c) the relative significance of acceleration and transport processes in the corona and interplanetary medium. An online (near-real-time) retrieval of the proton spectral index offers a direct way to monitor the evolution of the acceleration episode and supports operational nowcasting

of high-energy SEP conditions. The immediate hardness of the solar proton spectrum directly indicates whether a significant 50–100 MeV component exists. High abundance of this component suggests that the most dangerous high-energy particles can arrive within minutes, creating a narrow yet critical window for issuing alerts to safeguard satellite electronics and space infrastructure.

Traditionally, the energy spectrum of solar protons during GLEs has been inferred using the global Neutron Monitor (NM) network (Clem & Dorman, 2000; Mishev & Usoskin, 2016; Tylka & Dietrich, 2009). In this approach, the primary proton spectrum is reconstructed indirectly by fitting the count-rate increases observed at stations with different geomagnetic cutoff rigidities using model-dependent yield functions. The method relies on assumptions about the spectral form, angular distribution, and atmospheric cascade development, and provides only integral neutron count rates rather than direct energy information. The sensitivity of the NM network to higher-energy solar protons is fundamentally constrained by geomagnetic cutoff rigidity: while a few stations are located at rigidities exceeding ∼8 GV, the expected GLE-related enhancements at such high-cutoff sites are typically very small and often fall below the threshold of statistical significance. As a result, these stations cannot be reliably incorporated into the global inversion procedure, and the recovered spectra are dominated by responses from low- and mid-rigidity monitors. Consequently, the presence and temporal evolution of a hard, high-energy tail in the solar proton spectrum—critical for space-weather hazard assessment—remain poorly constrained by NM data alone (Asvestari et al., 2017).

In contrast, direct ground-based measurements of energy-dependent observables of secondary particles offer a complementary, more transparent physical diagnostic. Simultaneous measurements of muon and neutron energy, along with coincidence signals among different detector components, examine the multiplicity and compactness of secondary particle bundles produced by high-energy solar protons. These observables depend strongly on primary proton energy and allow event-by-event identification of high-energy interactions, expanding the sensitivity beyond the range accessible to the NM network. Such direct spectrometric and coincidence-based measurements thus provide a powerful way to estimate spectral hardness during GLEs with less reliance on global yield-function inversions and improved capacity for rapid space-weather diagnostics.

During a GLE, the enhancement of charged and neutral particle fluxes at the ground level is dominated by secondary muons and neutrons, with electrons and gamma rays contributing less (Grieder, 2001). Electromagnetic secondaries are produced copiously in the upper atmosphere through π^0 decay and cascade development. Electrons with energies below several tens of MeV are efficiently absorbed by ionization and bremsstrahlung losses, while gamma rays are attenuated by pair production and Compton scattering in the atmosphere. Muons are highly penetrating and constitute the dominant charged component at the ground level for primary proton energies above several GeV (Dorman, 2004).

In this work, we address a central limitation of traditional GLE diagnostics based on the neutron monitor network, where the recovery of the solar proton spectrum is indirect, model-dependent, and effectively constrained by geomagnetic cutoff rigidity, leaving the high-energy tail poorly resolved. This limitation motivates the use of detectors that provide not only count-rate enhancements but also energy-deposit spectra of secondary neutrons and muons at the ground level. We demonstrate that direct, energy-selective ground-based measurements of secondary particles, dominated during GLEs by muons and neutrons, provide a robust and physically transparent probe of primary proton energies. By exploiting energy thresholds and coincidence observables, this approach enables rapid estimation of spectral hardness and extends sensitivity to the most hazardous high-energy solar protons relevant for space-weather applications.

Earlier studies of the 20 January 2005 GLE 69, based on high-energy muon measurements at the same experimental site, reported a very hard solar-proton spectrum extending beyond 20 GeV (Bostanjan et al., 2007; Chilingarian, 2009; Gopalswamy et al., 2012) and introduced methods for estimating GLE hardness from ground-based observations (Chilingarian & Reymers, 2008; Zazyan & Chilingarian, 2009). The present work directly builds on those results, applying modern spectrometric and coincidence techniques to GLE 77 observed two decades later. This event offers a rare opportunity to extend earlier Aragats studies using improved instrumentation and to evaluate the hard, high-energy component of the solar proton population through the reconstructed spectra of secondary neutrons and muons.

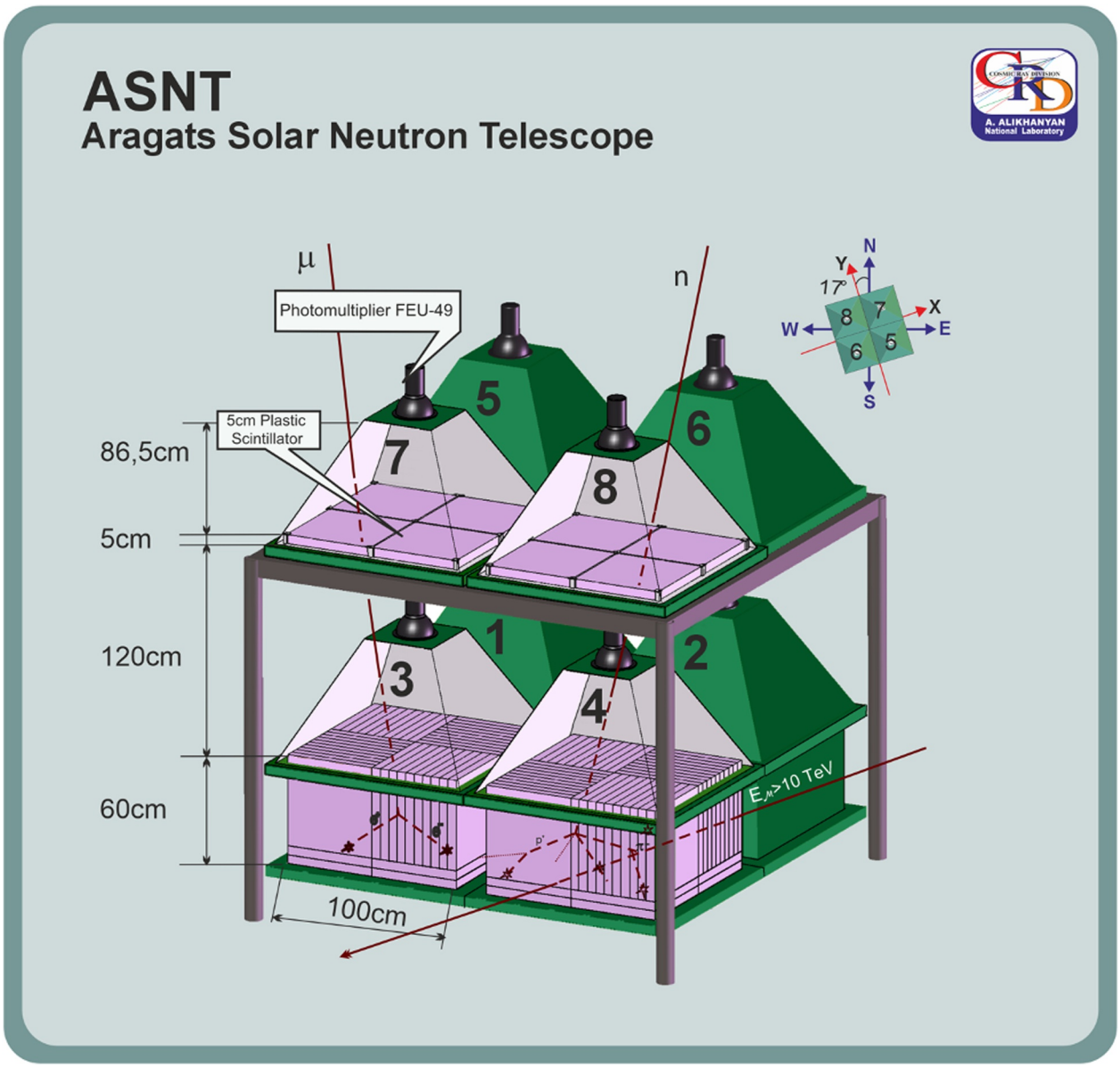

Figure 1. Assembly of Aragats Solar Neutron Telescope with the enumeration of 8 scintillators and orientation of detector axes relative to the North direction.

2. Instrumentation

2.1. ASNT Neutron/Muon Spectrometer

The ASNT can distinguish between neutral and charged particles (Chilingarian et al., 2007; Muraki et al., 2007). Its large 60-cm thick scintillator and logarithmic amplitude-to-digital converter (Logarithmic Amplitude-Digit Converter (LADC)) enable it to measure energy deposits from charged and neutral secondary particles produced in atmospheric cascades triggered by solar protons. Neutrons and gamma rays are detected indirectly through secondary charged particles produced in interactions within the thick scintillator, while the absence of signals in the upper veto scintillators is used to suppress charged particle contamination. ASNT consists of four identical modules, as shown in Figure 1. Each module includes forty scintillator slabs measuring $50 \times 50 \times 5$ cm^3, stacked vertically on a lower horizontal plastic scintillator slab measuring $100 \times 100 \times 10$ cm^3, forming a 60 cm thick, 1 m^2 area spectrometric layer (4 channels). Four scintillators, each measuring $100 \times 100 \times 5$ cm^3, are positioned above the main assembly to discriminate neutral particles by "vetoing" charged particles (another 4 channels).

The main ASNT trigger reads and stores analog signals from all 8 channels if at least one channel reports a signal above the threshold. The mean trigger frequency is ≈ 4 kHz, driven by the ambient population of cosmic ray (CR) species. The additional flux from GLEs usually does not exceed 5%–10%. However, during thunderstorm ground enhancements (TGEs; Chilingarian et al., 2010), the flux of gamma rays and electrons can reach up to 5 times the background level. The ASNT measurements include

1. Time series of count rates from all 8 channels of ASNT, with the integration time of the scintillators adjustable from 1 to 60 s.
2. Count rates of particles arriving from different incident directions: 16 possible coincidences between 4 upper and 4 lower scintillators. These coincidences allow to reconstruct the approximate arrival direction of penetrating particles.
3. Count rates of 8 special coincidences, such as one signal from the upper scintillators and one from the lower, or no signals in the upper with more than one in the lower, etc. All coincidences are recorded if signals occur within a 1-microsecond window.
4. Estimates of the variances of count rates for each ASNT channel, calculated from 12 five-second counts—meaning that in a minute, 12 sets of counts (each with a 5-second integration) are stored, and then means and variances are computed from these values.
5. An 8×8 correlation matrix of ASNT channels, calculated from five-second count rates over 1 min; the stored five-second time series are used each minute to monitor potential cross-talk between channels.
6. Each minute (after July 2012, every 20 s), histograms of energy deposits in all 8 channels of ASNT are recorded.
7. Similar data as in point 6 but only for particles not registered in the upper layer (veto on charged particles to select samples enriched by neutral particles).
8. Special triggers permit storing the traversal of horizontal muons within the acceptance ranges of 85–90° and 89.5–90°.

In this paper, we use information (4), (6), and (7) to reconstruct neutron and muon spectra during GLE 77. Raw histograms from pre- and GLE-intervals were constructed by subtracting the background histograms measured before GLE:

$$N_{\text{excess}}(E) = N_{\text{signal}}(E) - N_{\text{background}}(E)$$

Statistical uncertainties are Poisson-based:

$$\sigma(E) = \sqrt{N_{\text{signal}} + N_{\text{background}}}$$

During multiyear operation, we carefully monitor the count rates of each of the 4 ASNT channels to ensure the stability of the PM high-voltage supply and other electronic components.

In Figure 2, we present ASNT's registration of GLE 77 on 11 November 2025 (“01” coincidence, signal only in a 60 cm thick scintillator, all particles). All 4 independent channels show coherent observations of 2 peaks at 10:26-10:38 and 10:46–10:57.

2.2. SEVAN Light Spectrometer

SEVAN Light (Space Environment Viewing and Analysis Network, Chilingarian et al., 2009, 2024a, 2024b) is a compact, energy-deposit-resolving particle spectrometer that can separate neutral components (neutrons, γ-rays) from charged components (muons, electrons) of GLEs and TGEs (Chilingarian, Karapetyan, Sargsyan, Asatryan et al., 2024). SEVAN Light detectors installed at Aragats (3,200 m) include a 0.25 m^2 spectrometric scintillator with a 20 cm thickness and a 1 cm thick, 1 m^2 veto scintillator (see Figure 3), with an energy threshold of 5 MeV. The detector incorporates high-dynamic-range logarithmic ADCs (LADCs) to measure deposits of 5–300 MeV and coincidence logic to classify events as charged or neutral particles. The vertical coincidence window is 1 μs, effectively separating accidental coincidences. SEVAN detectors are among the few instruments capable of simultaneously measuring count rates and energy spectra of both charged and neutral cosmic ray species. The list of available information from SEVAN Light is as follows:

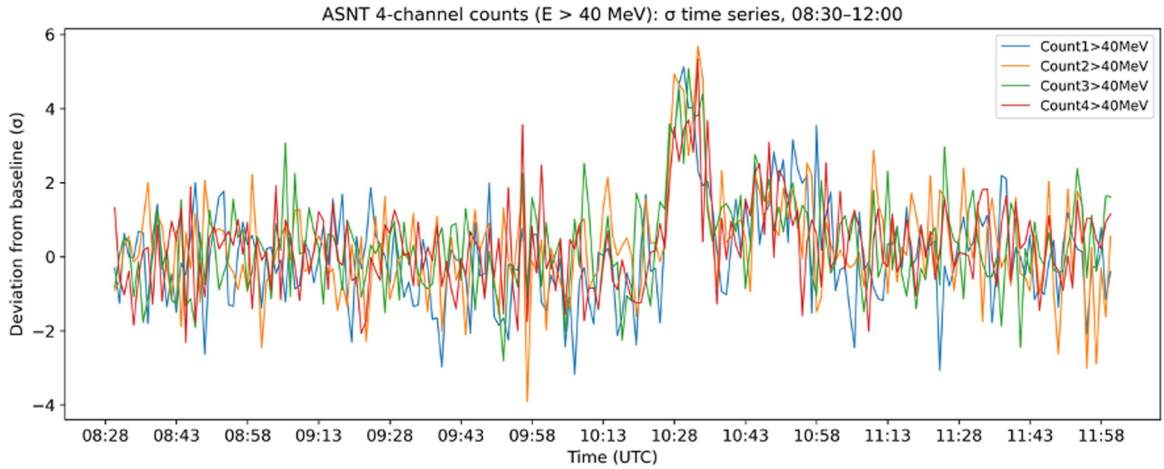

Figure 2. Uniformity of Aragats Solar Neutron Telescope (ASNT) time-series during registration of Ground Level Enhancement (GLE) 77. Each of 4 ASNT channels demonstrates uniform detection of GLE particles.

- 1-minute count rates of stacked 1 and 20-cm thick scintillators.
- 1-minute count rates of the coincidences "01", signal only in the 20-cm scintillator, "10"—signal only in the upper 1-cm thick scintillator; and "11"—signal in both scintillators.
- Histograms of energy deposits in both scintillators. Histograms corresponding to the coincidences mentioned above are stored continuously.

The samples selected by the "01" coincidence, which generate a signal in the lower scintillator but no signal in the upper, will be enriched in neutral particles. The samples selected by the "11" coincidence will be enriched in charged particles. In addition, the "10" coincidence will select mostly low-energy charged particles that stop before reaching the lower scintillator.

Although the SEVAN Light area is 16 times smaller than that of ASNT, it provides nearly 100% of the charge-particle veto because the veto scintillator area exceeds the spectrometric one. ASNT cannot achieve full coverage because the spectrometric scintillator is 60 cm thick, and muons hitting it at large zenith angles can mimic neutrons ("01" coincidence). This happens because inclined muons may bypass the upper veto scintillators while depositing energy in the thick spectrometric layer. This effect is minimal for vertically incident TGEs, but particle cascades initiated by solar protons can arrive at oblique angles, contaminating the neutron flux. Our calculations indicate that 3%–5% of the neutral flux during GLE may be due to inclined muons.

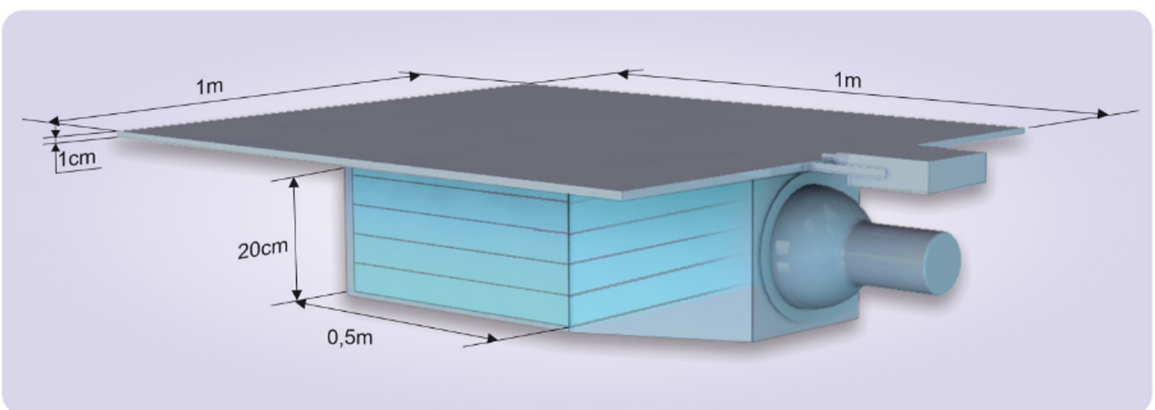

Figure 3. Setup of SEVAN Light detector. 20-cm thick 0.25 m^2 area spectrometric scintillator and 1-cm thick, 1 m^2 area "veto" scintillator.

2.3. Recovery of Energy Spectra

In this subsection, we describe a method for recovering energy spectra from energy deposit histograms (see details in Chilingarian, Hovsepyan, Karapetyan, Sargsyan, & Chilingaryan, 2022; Chilingarian, Hovsepyan, Karapetyan, Khanykyanc et al., 2022; Chilingarian, Hovsepyan, Karapetyan, Kozliner et al., 2022). These histograms display the number of events versus the energy deposited in the detector. The LADC, used in MAKET and SEVAN Light electronics, allows for the acquisition of spectra up to 300 MeV. The LADC applies a logarithmic function to the input signal, meaning that the quantization step size varies depending on the input signal's amplitude. This enables the LADC to handle a wide dynamic range of input signals by compressing higher-amplitude signals and expanding lower-amplitude ones.

To determine the original energy spectrum from the measured energy deposit, we solve the inverse problem. This task is complex because cosmic ray interactions and detection processes distort the original energy distribution. Estimating the detector's response function generally involves predicting outcomes for a known set of inputs (solving the direct problem). The response function describes how a detector responds to different particle fluxes at various energies, indicating the probability of measuring energy deposit E_{dep} if the true energy is E_{true}. Particle fluxes at any geographic coordinates and altitudes were obtained from the EXPACS web calculator (Sato, 2016). The GEANT4 code (Agostinelli et al., 2003) was used to simulate particle transport through different media, accounting for various sources of randomness and measurement uncertainties. Consequently, the response matrix includes the smearing effects caused by the detector's finite resolution and the asymmetry in bin-to-bin migration due to steep cosmic ray spectra. The energy deposit in the detector simulated with GEANT4 was converted into LADC codes using the following expression:

$$[k] = d \cdot \ln \frac{E_{dep}}{E_0} + k_0 \tag{1}$$

where $(k) \geq 1$ is the LADC code, $d \approx 10.5$ is the LADC scale factor, E_{dep} is the energy release in the scintillator, E_0 is the average muon energy release in the plastic scintillator, and k_0 is the LADC code corresponding to the energy loss of a minimum-ionizing particle in the detector.

As a result of simulation trials, we obtain the response matrix A_{ij}, which shows how simulated particles with input energy x_i ($i = 1, N$) are distributed across bins y_j (the number of simulated events falling into energy bin I after processing by the detector response):

$$y_j = \sum_{i=1}^{N} A_{ij}\, x_i, i = 1, \ldots, N. \tag{2}$$

The energy deposit E_{dep} (MeV) was simulated for a given set of energies E_j ($j = 1, N$) spanning an energy range from 1 to 300 covered by $N = 127$ energy bins. Conversion of energy to LADC codes was performed according to Equation 1. $M = 10^5$ events were simulated for each E_j. For each true-energy bin E_i, $M = 10^5$ events were simulated. The response matrix row A_{ij} was normalized by M. After normalization, A_{ij} represents the probability that a particle with true energy in bin i is detected in bin j. To retrieve the actual energy spectrum from the measured energy deposit histogram, that is, estimate x from y, we applied an unfolding procedure based on inversion of the response matrix.

Because the response matrix in the chosen binning was sufficiently well-conditioned, we used direct inversion to obtain the differential energy spectrum:

$$x_i = \sum_{j=1}^{N} \left(A^{-1}\right)_{ij} y_j, i = 1, \ldots, N. \tag{3}$$

We used this method to recover the energy spectra of electrons and gamma rays from large particle bursts observed on Aragats. Electrons in EASs entering the strong electric fields of thunderstorms accelerate and form relativistic runaway avalanches, which, when registered on the Earth's surface, can enhance the background by a factor of 10 or more. Several spectrometers on Aragats measured the energy spectra of the TGE that occurred on 6

Table 1
Purity of the "11" Coincidence Observed by SEVAN Light Spectrometer

Energy of solar protons (GeV)	mu±	e±	gamma	%
10	60	30	10	100
15	48	41	11	100
20	48	41	11	100

Note. Thus, ≈90% of the "11" selected particles are charged particles, including muons and electrons, with ≈10% contamination from gamma rays. We ignore contamination from neutrons and protons here.

October 2021 (Chilingarian et al., 2010, 2011). The TGE spectra were recovered by ASNT, large (12 × 12 × 30 cm) NaI (Tl) spectrometers (Chilingarian et al., 2015), and SEVAN Light. In Figure 12 of Chilingarian, Hovsepyan, Aslanyan, et al. (2023), the differential energy spectra of a large TGE on 6 October 2021, were compared, and all three reconstructed energy spectra agree reasonably well. The differential energy spectra of gamma rays and electrons were approximated using a five-parameter fit, including the spectral knee position (Chilingarian, Hovsepyan, Karapetyan, et al., 2023).

2.4. Comparison of Simulated and Experimental Events

The comparison between experimental and model data was performed using the CORSIKA and GEANT4 models, applying the same analysis procedures for both experimental and simulated particles. CORSIKA (COsmic Ray SImulations for KAscade) simulations involved mono-energetic primary protons entering the atmosphere. These simulations used CORSIKA version 7.7500 (Heck et al., 1998), incorporating the QGSJETII-04 (Ostapchenko, 2024) and URQMD models for hadronic interactions and the EGS4 package for electromagnetic interactions. The simulations employed fixed-energy proton beams at 7.3,10, 15 and 20 GeV, injected within a narrow cone with an opening angle of 30°, distributed according to $\cos^2\theta$ and a uniform azimuthal distribution. Secondary particles were recorded at an observation level at an altitude of 3,200 m above sea level, matching the elevation of the Aragats research station. The energy thresholds for muons, electrons, and gamma rays in CORSIKA were consistent with the effective detection thresholds of the SEVAN instruments and did not influence the comparison. However, the neutron threshold in CORSIKA is too high. Therefore, directly computing the muon-to-neutron ratio, which is comparable to the experimental observable, is not feasible in the current CORSIKA configuration. The low-energy neutron component, which dominates the detected signal, lies below the simulation's hadronic tracking threshold (∼300 MeV). Moreover, the experimental neutron signal is defined by energy deposition from secondary interactions in the detector, rather than by the neutron's kinetic energy. For these reasons, we treat the neutron spectrum and the μ/n ratio as phenomenological observables constrained by data (data-driven observables), while the muon component ("11" channel) is used for direct comparison with CORSIKA-based simulations. Meanwhile, neutral-particle (neutron) spectra were obtained from detector data and analyzed physically, but were not directly compared with the primary-energy template library. All simulated secondary particles hitting the upper detector plane were propagated using the GEANT4 full detector response modeling.

The resulting modeled histograms were processed with the same energy-spectrum recovery and analysis procedures used for the experimental data (see Section 2.3). Finally, events fulfilling the '11' coincidence were selected; this channel is muon-dominated but contains electrons and gamma contamination, as quantified in Table 1. Corresponding muons were summed, and the generation of new showers from solar protons continued until the total number of charged particles reached the experimentally observed "11" coincidence.

The "11" coincidence channel is predominantly governed by muons and electrons, produced by muons, with a minor contribution from neutral particles. Since neutrons mainly deposit energy through secondary recoil processes, which have a low probability in thin plastic scintillators, their contribution to the "11" coincidence channel is also insignificant compared to that of penetrating charged particles. As we mentioned above, CORSIKA did not track hadrons in cascades below 300 MeV, so we only present other secondaries involved in the "11" coincidence; see Table 1. In Table 1, we show the percentages of different particle types that account for the "11" coincidence count rates for proton showers of 10, 15, and 20 GeV.

The GCR background b_j in each of the $J = 127$ energy bins was calculated using the EXPACS code (Sato, 2016). Secondary muons, electrons, gamma rays, and others at 3,200 m were folded with the detector response to select the same "11" coincidences (muons). Then, GLE enhancements in each bin and at the minute t of GLE were calculated:

$$\mathrm{gle}_j\,(t) = \exp_j(t) - b_j, j = 1,127$$

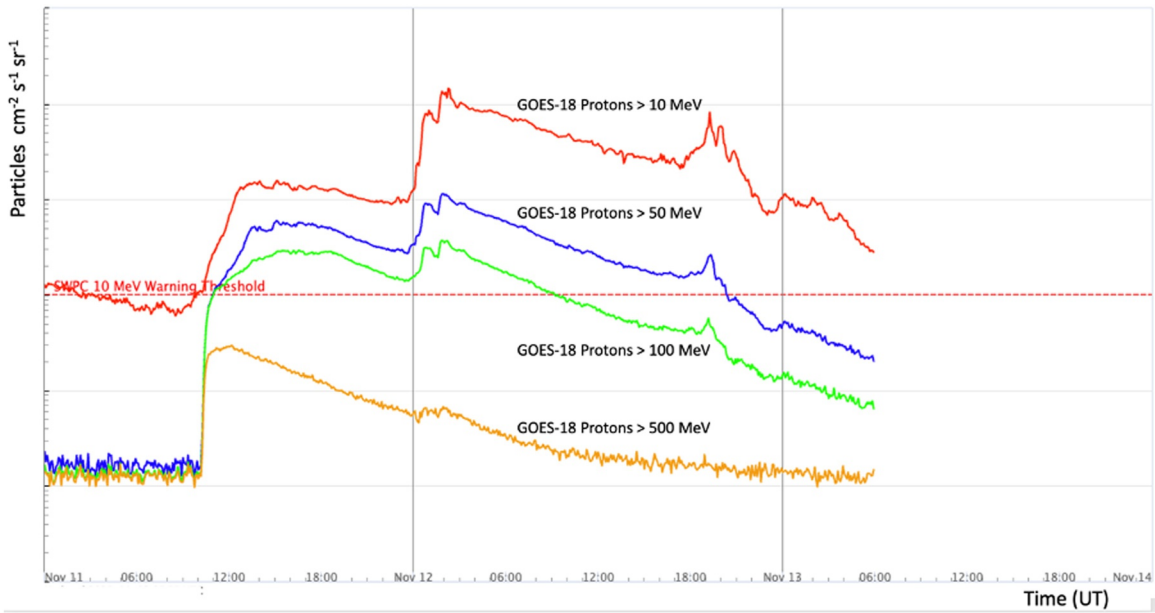

Figure 4. Solar energetic proton event associated with Ground Level Enhancement 77 as measured by GOES-18. The figure shows time profiles of integral proton fluxes above 10, 50, 100, and 500 MeV.

Where $\exp_j$ are observed muons in energetic bins of the recovered differential energy. The total GLE enhancement was summed over the full set of bins and over the whole GLE time. We assume that the background was constant during GLE.

$$\mathrm{GLE} = \sum_{t1}^{t2} \sum_{j=1}^{J} \mathrm{gle}_j\,(t),$$

In this study, we sum GLE minutes around 2 pronounced peaks in the SEVAN Light time series, with the following start and end times: $t1$ = 10:26, $t2$ = 10:38 for the first peak, and $t1$ = 10:41, $t2$ = 10:51 for the second peak. Thus, we will use the glej notation without explicitly mentioning the time dependence.

For each tested monoenergetic primary energy E_i, the simulated template $y_j(E_i)$ provides the accumulated count number in each bin j. We tested 4 primary energies: 7.3, 10, 15, and 20 GeV. To align simulation and experiment on the same scale, we first identify the total event enhancement and use it to normalize the simulations. The simulations stopped when the total enhancement, summed over all j bins and over minutes of GLE (separately for peak1 and peak 2), reached the experimental GLE value. The model event amplitude is represented by $\mathrm{N_{sol}}(E_\mathrm{i})$, that is, the number of primary solar protons with energy E_i needed to reproduce the observed GLE enhancement. This procedure guarantees that all tested E_i values produce the same total GLE enhancement. Thus, monoenergetic proton simulations generate response templates for different primary energies E_i. After normalizing to the same total enhancement, these templates mainly differ in their spectral shapes and high-energy tails. Consequently, the best-fit model (E_0) should be selected based on differences in spectral shape. The spectral shape of secondaries induced by low-energy protons will tend to produce lower-energy secondaries, whereas high-energy protons will produce heavier tails. The full monoenergetic CORSIKA template comparison was performed only for the charged '11' channel. Neutron data were used as an independent phenomenological constraint through the temporal shape and the μ/n ratio.

3. GLE 77: GOES, NM, and ASNT Evidence

The GLE 77 event on 11 November 2025, followed an X5.1-class solar flare with a soft X-ray peak at 10:04 UTC, as measured by the GOES soft X-ray sensors. The proton channels of the GOES-18 spacecraft (Jarry et al., 2026; Kress et al., 2020) showed a rapid increase in intensity starting at 10:15, approximately 10 min after the flare peak

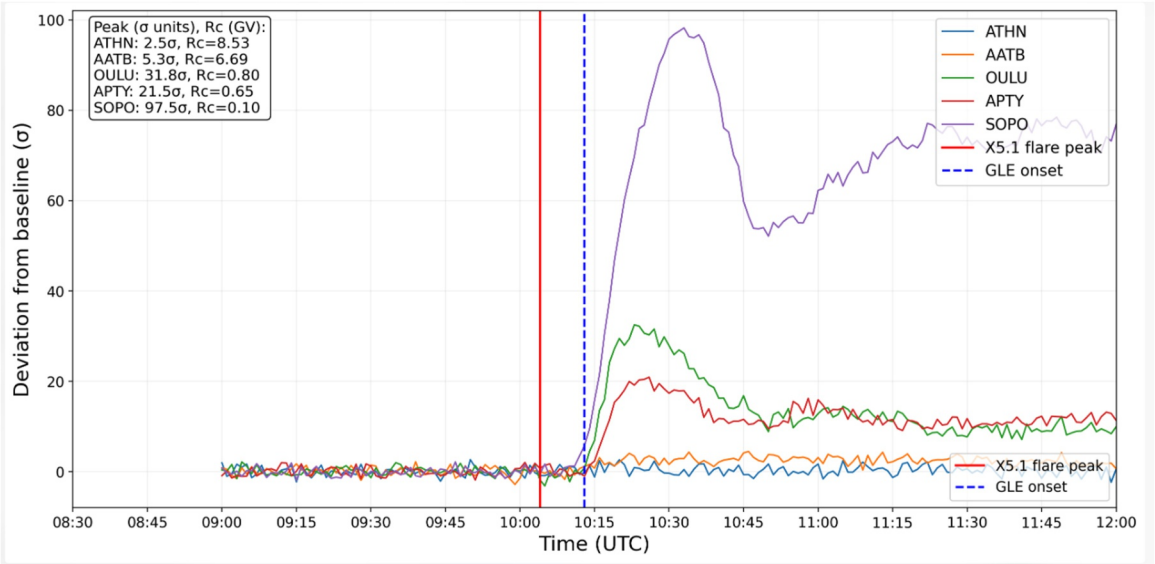

Figure 5. Time series of neutron monitor responses during Ground Level Enhancement (GLE) 77, expressed in units of σ relative to the pre-event baseline. Data are shown for stations spanning a wide range of geomagnetic cutoff rigidities: South Pole (SOPO), Oulu (OULU), Apatity (APTY), Almaty (AATB), and Athens (ATHN). The event onset occurred at approximately 10:12–10:14 UTC, with the strongest enhancements observed at high-latitude stations with low cutoff rigidities. Dashed vertical lines mark the onset time of the solar flare and the beginning of the GLE.

(Figure 4), indicating the arrival of high-energy solar protons at 1 AU under nearly scatter-free propagation conditions. The enhancement of the >50 MeV proton flux reaches a 10-fold increase at 10:20, and a 100-fold increase at 11:55.

Neutron monitors (NMs, Dorman, 2004; Mishev & Usoskin, 2020) and the SEVAN network detected the onset of GLE 77 at 10:12–10:14 UTC (Mishev et al., 2026). The peak response varied strongly among stations, reflecting their different geomagnetic cutoff rigidities and the anisotropy of the SEP flux. Figure 5 presents the time series of neutron flux enhancements expressed in units of standard deviation (σ) relative to the pre-event baseline, for a set of neutron monitors spanning a wide range of latitudes: South Pole (SOPO), Oulu (OULU), Apatity (APTY), Almaty (AATB), and Athens (ATHN). As expected, high- and low-latitude stations with low cutoff rigidities exhibit the largest enhancements, reaching nearly 100σ at the South Pole, whereas mid- and low-latitude stations show much smaller responses and do not reproduce the pronounced double-peak structure observed at polar stations.

To highlight the hardest part of the secondary particle flux, we generated a time series of neutrons and muons using only events with deposited energy above 40 MeV. This threshold reduces the low-energy background, reduces contamination from soft electromagnetic secondaries, and enhances sensitivity to particles produced in the most energetic atmospheric cascades. Consequently, the selected samples are more directly linked to the high-energy end of the solar proton spectrum. The downside is that the measured time profiles no longer reflect the entire secondary flux but only its more energetic component.

Figure 6 shows the time series of the neutron count rate (coincidence "01") recorded by the ASNT detector for energies above 40 MeV, expressed in units of σ. A clear and statistically significant response exhibited a pronounced enhancement starting ≈20 min after the flare, with a first maximum reaching approximately 11σ during 10:26–10:38 UTC, followed by a secondary peak of about 7σ during 10:45–10:54 UTC. The presence of two distinct peaks is consistent with the double-peak structure observed in polar neutron monitors and reflects the temporal evolution of the high-energy solar proton flux reaching the atmosphere.

Thus, the >40 MeV selection should be interpreted as a hardness filter: It increases sensitivity to relativistic solar protons while reducing sensitivity to the softer component of the event. In addition to neutron measurements, ASNT observed a statistically significant increase in the muon component during GLE 77, with a time structure similar to the neutron enhancement (see Figure 7).

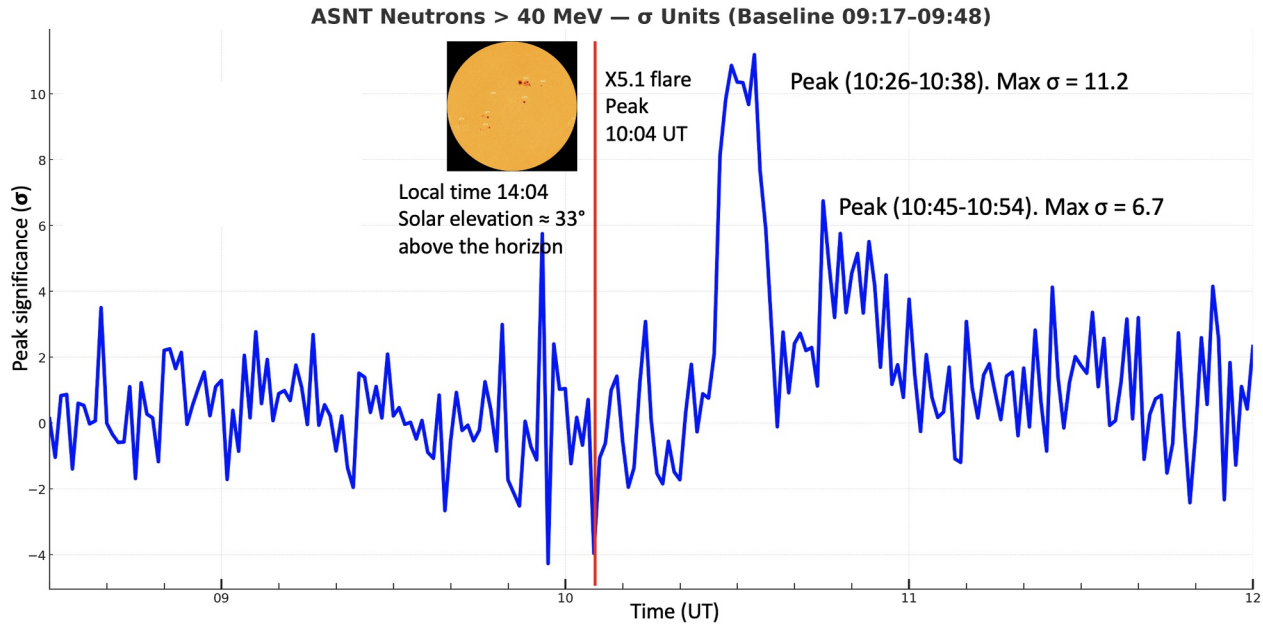

Figure 6. Time series of the Aragats Solar Neutron Telescope (ASNT) neutron response (coincidence "01") for energies above 40 MeV during Ground Level Enhancement 77, expressed in units of σ. The vertical red line marks the time of the X5.1-class solar flare peak at 10:04 UTC. Two pronounced enhancements were observed in the ASNT neutron signal, with a primary maximum of approximately 11σ during 10:26–10:38 UTC and a secondary peak of about 7σ during 10:45–10:54 UTC, indicating a sustained flux of high-energy solar protons reaching the ground level.

Muon enhancement indicates the presence of sufficiently energetic primary solar protons capable of producing penetrating secondary muons at the ground level. Because high-energy secondary muons are more likely to be produced by higher-energy primary protons, the muon response offers independent confirmation of the spectral hardness inferred from the neutron monitor network and provides a direct local basis for the spectral reconstruction discussed in the next section. Unlike neutron monitor counts, which reflect a rigidity-integrated response, ASNT features an energy-deposit registration capability that allows the selection of different energy domains and increases sensitivity to the high-energy tail of the atmospheric cascade. Significantly, ASNT delivers simultaneous neutron and muon measurements at the same location under identical atmospheric and geomagnetic conditions, enabling consistent cross-validation of the GLE timing and intensity across secondary components.

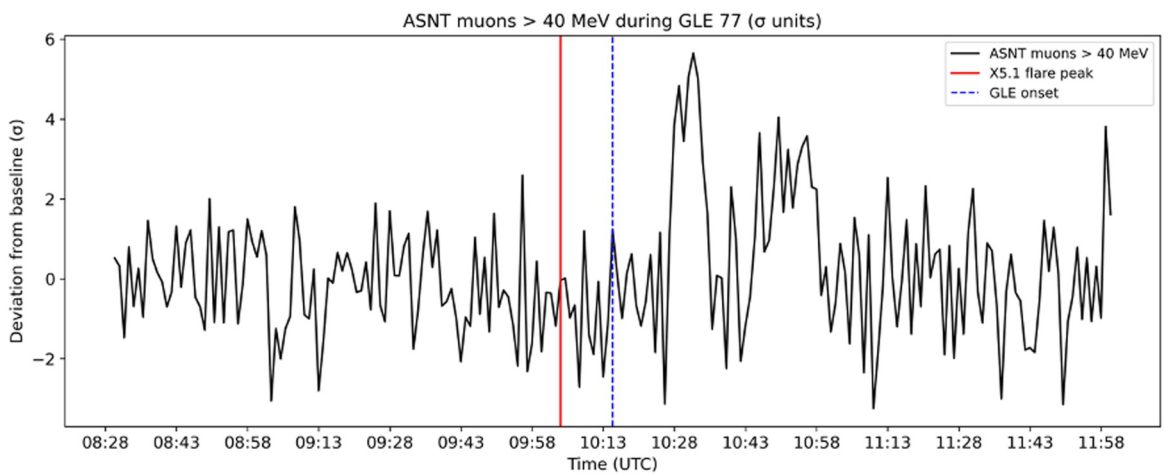

Figure 7. Time series of Aragats Solar Neutron Telescope muon counts above 40 MeV during Ground Level Enhancement (GLE) 77 shown in units of σ. The red vertical line indicates the soft X-ray peak time of the related X5.1 solar flare (10:04 UT), and the dashed blue line marks the GLE onset time inferred from the neutron monitor network.

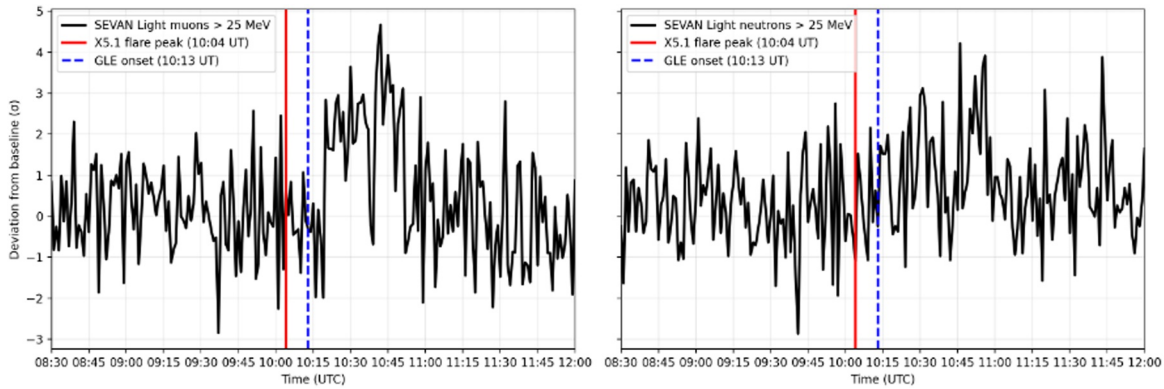

Figure 8. Time series of SEVAN muon (coincidence "11") and neutron (coincidence "01") counts above 25 MeV during Ground Level Enhancement (GLE) 77, presented in units of standard deviations from background (Nσ). The red vertical line marks the soft X-ray peak time of the associated X5.1 solar flare (10:04 UT), and the dashed blue line indicates the GLE onset time.

GOES-18 recorded a rapid rise in the higher-energy SEP proton channels following the X5.1 flare, while neutron monitors across a wide range of geomagnetic cutoff rigidities displayed a clear ground-level response starting at 10:12–10:14 UT. At Aragats, ASNT observed increases in both neutron and muon channels, and the timing matches the multi-peak pattern seen at polar neutron monitor stations. Possibly, an impulsive, hard, and well-collimated proton beam was emitted early in the event and reached Earth with minimal pitch-angle scattering, creating the strong initial response observed by high-latitude neutron monitors. The lack of a clear impulsive-phase signal at Aragats may reflect not only the anisotropy of the initial proton beam but also the limited statistics. A second event, roughly 10 min later, might have been less intense, leading to a weaker secondary response. The two-peak structure has also been discussed in (Agarwal et al., 2026), where GLE 77 is described as one of the hardest, and the double peak is interpreted as evidence for two distinct particle populations.

4. GLE 77: Comparison of the 2 Separate Peaks

Because the sensitive area of SEVAN Light is much smaller than that of ASNT, the SEVAN time series in Figure 8 uses a lower threshold of 25 MeV to improve counting statistics. The second peak appears somewhat more pronounced, and the pause between peaks is less distinct than in ASNT. These differences are most likely due to lower statistics, different thresholds, and detector response differences rather than a physical discrepancy in the particle flux. The agreement in timing with ASNT and with the established GLE onset confirms the solar origin of the SEVAN signal.

In Figure 9, we present the recovered differential energy spectra of muons (coincidence "11") and neutrons (coincidence "01") of the first and second peaks of GLE 77.

For charged particles, the energy spectrum is primarily shaped by track geometry in the scintillator. The 5–20 MeV region is populated by marginally charged events: short tracks from particles that cross the detector only partially, releasing less energy than a fully penetrating muon. The broad 40–70 MeV hump in muon spectra is a characteristic signature of single through-going muons in the 20 cm scintillator. A nearly vertical muon deposits about 40 MeV, while an inclined muon travels a longer path, shifting the energy deposit toward higher energies and broadening the hump. At higher deposited energies, the charged spectra include rarer events such as strongly inclined muons and close muon pairs or triples.

Neutron energy spectra have different origins and therefore different shapes. Neutrons do not directly ionize; they are detected only through secondary charged particles produced in neutron interactions with the scintillator and the surrounding material. Its monotonic hard spectrum means there is no preferred single-track energy-deposit scale, unlike the muon hump. Instead, each detected neutron event reflects a stochastic nuclear interaction that can produce recoil protons, charged fragments, or secondary cascades with a wide range of energies released. Because of this interaction-driven origin, the neutron spectrum decreases smoothly and monotonically, extending to higher deposited energies through occasional strong local interactions. Thus, the charged spectra are dominated by the

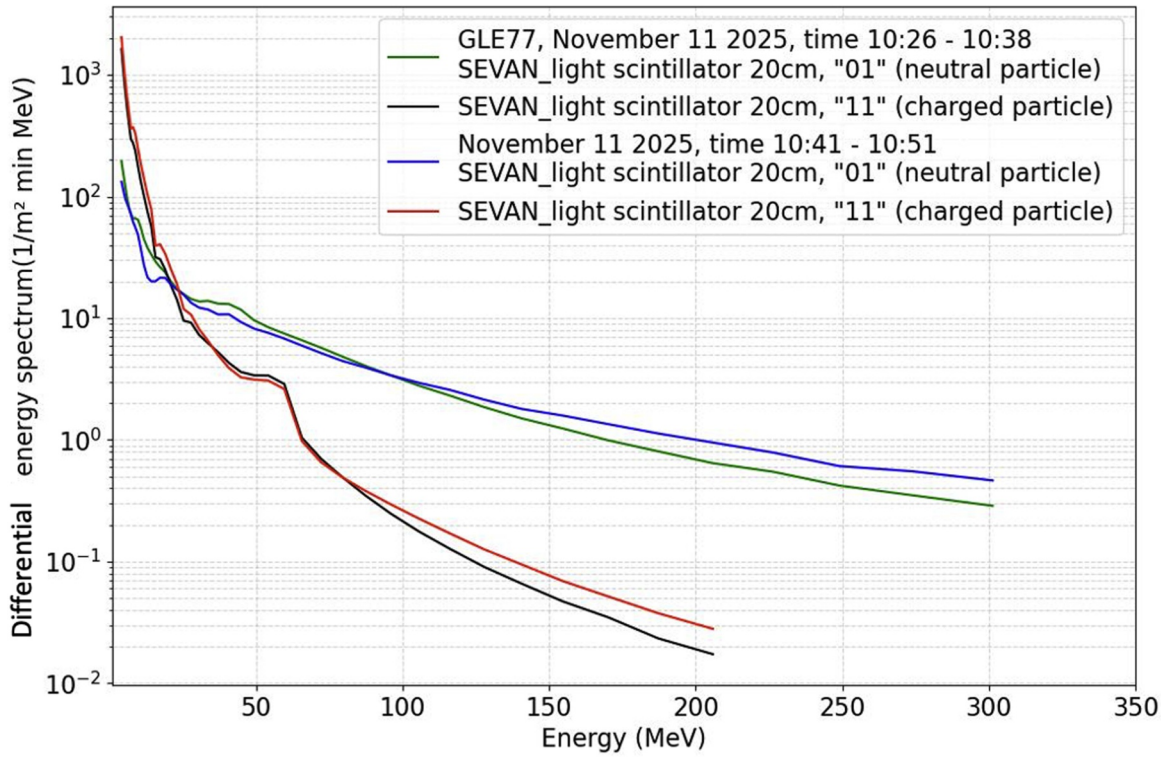

Figure 9. Recovered differential energy spectra for muons and neutrons for peaks 1 and 2.

geometrically defined response of single muons, whereas the neutron spectra are dominated by the broad response of nuclear interactions.

This contrast is important because maintaining a broader high-deposit muon branch requires sufficiently high energetic meson production in the atmosphere, whereas neutron-induced energy deposits can remain significant without creating an equally long-lasting muon deposit tail. If the solar-proton spectrum had included a substantially harder component extending well above the local cutoff, the muon spectra would have stayed flatter. Instead, the observed trend shows the opposite: the muon branch steepens early and significantly, while neutrons maintain a long residual tail.

The contrast becomes even clearer when compared with earlier Aragats muon studies of GLE 69 (20 January 2005). For that event, observations at Aragats using high-energy muon channels indicated the presence of primary solar protons with energies exceeding 20 GeV, demonstrating a hard, extended primary spectrum well above the geomagnetic cutoff. Such high-energy protons efficiently produced penetrating muons, resulting in comparatively flatter secondary spectra at high energies. In contrast, the muon spectrum observed during GLE 77 steepens rapidly above ∼60 MeV, indicating the absence of a substantial high-energy proton component (Balabin et al., 2026). This difference highlights the fundamentally different nature of the two events: GLE 69 was driven by a powerful accelerator capable of producing protons with >20 GeV, whereas GLE 77 was dominated by near-cutoff solar protons and represents a significantly weaker acceleration episode. Figure 10 displays the muon-to-neutron ratios for both peaks. The ratios are sensitive to the relative efficiencies of hadronic neutron production and meson production followed by decay in atmospheric cascades. In GLE 77, ratios decrease rapidly with energy, showing that the muon component fades much faster than the neutron component. This imbalance suggests that the cascade continues to effectively produce hadronic neutral secondaries but does not maintain a similarly strong penetrating muon branch. Such behavior aligns with what is expected for a cutoff-limited or only moderately super-cutoff SEP population.

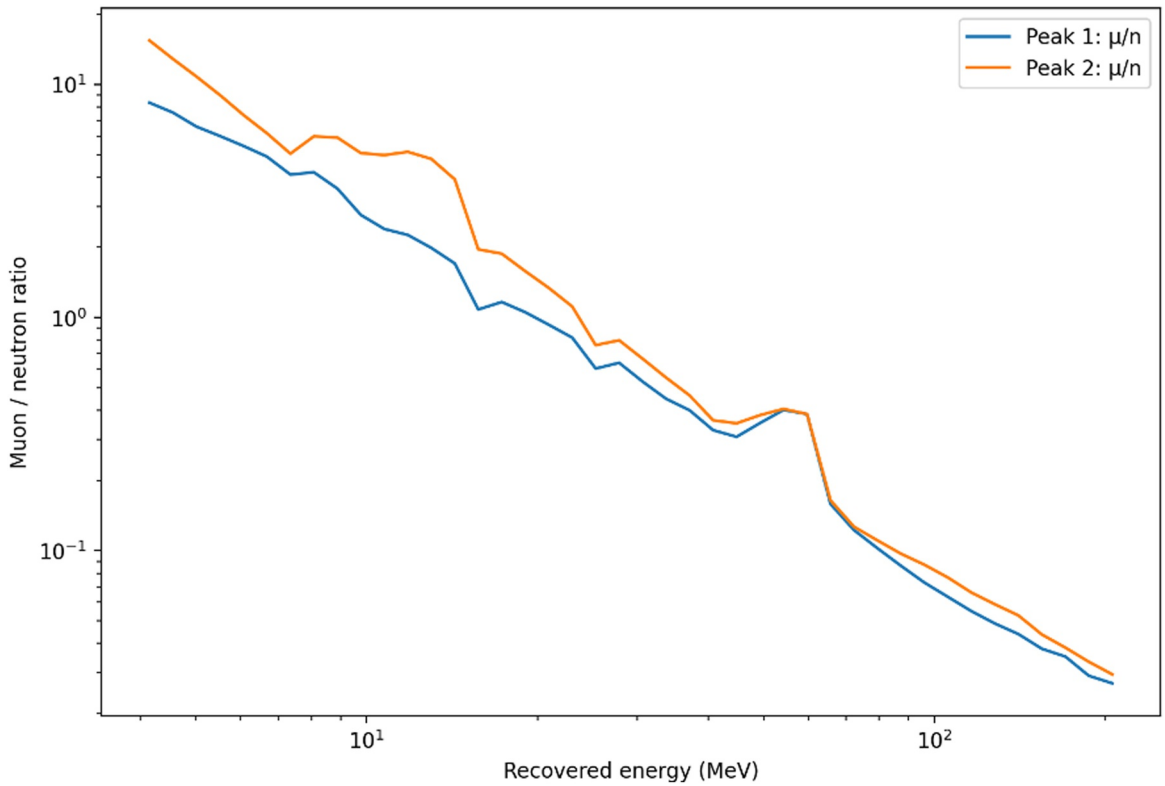

Figure 10. Muon-to-neutron ratio in the 10–200 MeV recovered energy range during Ground Level Enhancement 77.

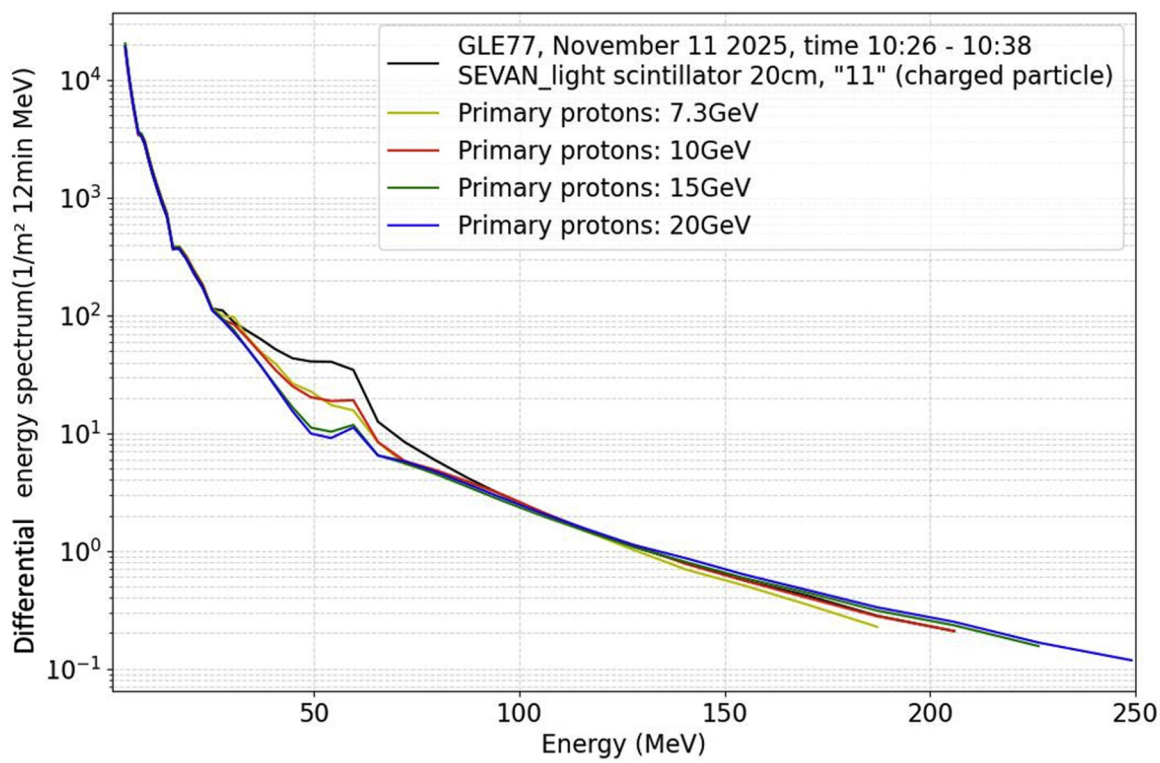

Figure 11. Recovered differential energy spectra of the Ground Level Enhancement muon-dominated component (black) and the four monoenergetic simulations.

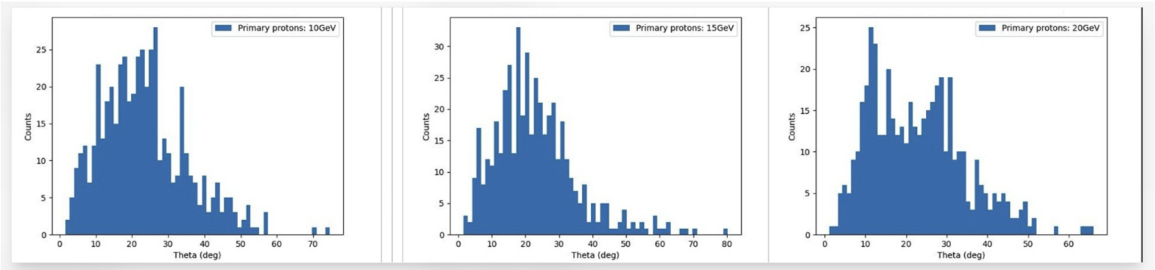

Figure 12. Simulated charged particle angular distributions at detector entry for the 10, 15, and 20 GeV simulations. All three show substantial broadening relative to the primary proton injection (0°–30°) at the top of the atmosphere. The distribution shapes reflect the mixture of muon and electron populations reaching the detector with different angular histories after cascade development.

5. Analysis of Muon Energy Spectra: Comparison With Simulations

The simulated scheme, with its limitations is described in detail in Section 2.4. In Figure 11, we show the experimental and four simulated spectra of the "11" muon-dominated coincidence of the SEVAN Light spectrometer. As shown in the previous section, the recovered energy spectra of both GLE peaks differ only slightly; therefore, we will base our analysis solely on peak 1 data.

The spectrum can be divided into four energy regions. The 10–20 MeV range is a common low-energy-deposit region where the experimental and all model curves nearly overlap. Above 20 MeV, the experimental spectrum diverges upward from the common low-energy branch earlier than the 15 and 20 GeV simulations; that is, the experiment stops its monotonic decline much sooner, while the 15 and 20 GeV templates continue decreasing until higher deposited energies. Curves corresponding to lower primary energies decline more slowly. The experiment then shows a prominent 40–70 MeV hump, whereas the simulations display only weak shoulders. Finally, the tail above 100 MeV constrains the rarest and largest deposits. In the transition and hump regions, the 7.3 and 10 GeV cases are noticeably closer to the experiment than the 15 and 20 GeV cases. In the tail region, the measured spectrum is shorter than the 15 and 20 GeV templates and more comparable in extent to the 7.3 and 10 GeV cases. Below, we describe these 4 regions in more detail.

5.1. Region I: 10–20 MeV

This interval is the only one where the experiment and all simulations match almost exactly. It is the least discriminating part of the spectrum: low-energy particles (electrons and gamma rays) produce small deposits here, and the muon deposit is influenced by short effective track lengths rather than by the initial proton energy. Therefore, the coincidence at 10–20 MeV indicates only that the near-threshold part of the charged response is universal.

5.2. Region II: 20–25/30/50 MeV Transition

The real difference starts above 20 MeV. The experimental spectrum stops the sharp decline after 25 MeV. The spectra corresponding to 7.3 and 10 GeV primaries repeat this tendency after 30 MeV, and the spectra of 15 and 20 GeV show a sharp decline until 50 MeV. This shows that, in high-energy simulations (15 and 20 GeV), the spectrum is dominated by higher-energy deposits and a deficit of low-energy particles (below 50 MeV). Thus, this region shows that the experimental spectrum is closer to those of lower-energy primary protons.

5.3. Region III: 40–70 MeV Hump

The 40–70 MeV hump is the primary signature of single-muon deposits in the 20-cm scintillator. Its strong amplitude in the experiment indicates that the actual shower delivers a richer population of muon trajectories to the detector than the monoenergetic templates suggest. The shortfall across all simulations in this region reflects both the underrepresentation of partial crossings and the incomplete sampling of the full population of muon trajectories reaching the detector. The deposited energy roughly scales as $Edep \approx (dE/dx) \times t/\cos\alpha$, where $t = 20$ cm is the scintillator thickness and α is the angle of incidence relative to the detector normal. Therefore, once the detector-entry angular distribution is broadened by atmospheric cascade development (see Figure 12), the vertical single-muon response near 40 MeV broadens into a 40–70 MeV hump.

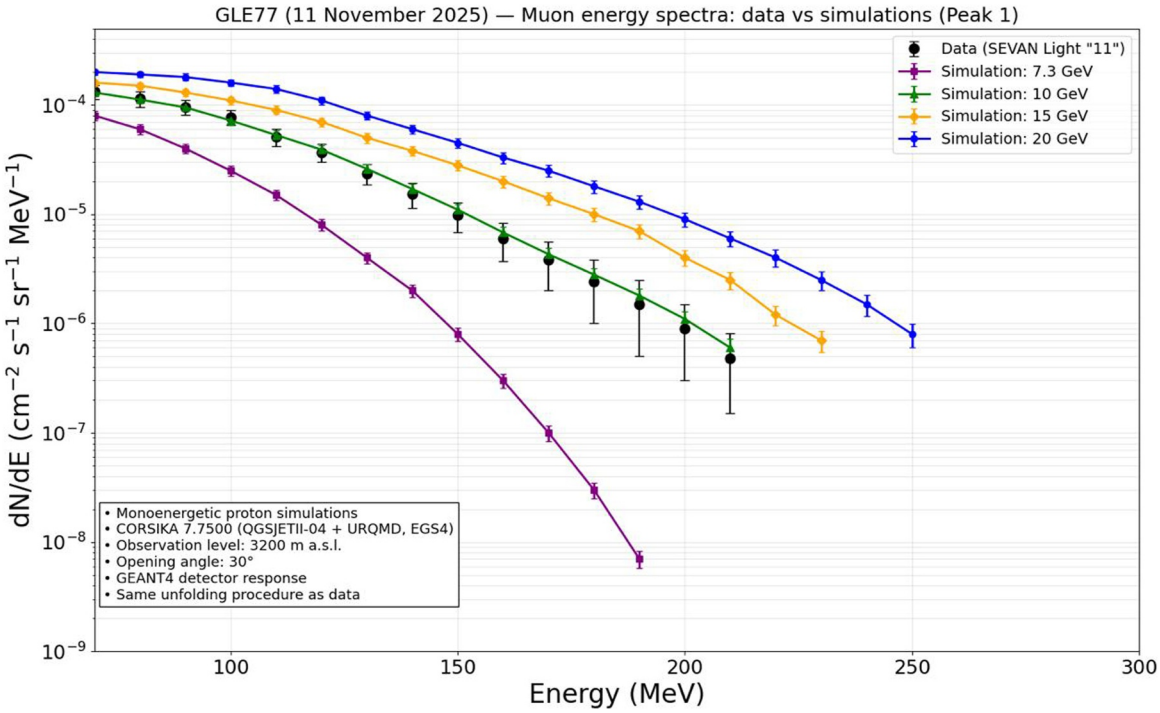

Figure 13. Zoomed-in high-energy tails of the experimental (black) and simulated differential energy spectra. Error bars are statistical.

Thus, the vertical single-muon response near 40 MeV is naturally broadened into a 40–70 MeV hump once the detector-entry angular distribution is broadened by atmospheric cascade development, while deposits above 70 MeV reflect progressively rarer and more complex energy-deposit events. The lower-energy spectra are again closer to the experiment than those for higher-energy primaries.

5.4. Region IV: Hard-Tail Extension (>100 MeV)

Energy spectra above 100 MeV can arise from multiple charged particles passing through the detector within the detector's resolving time, local electromagnetic sub-showers, or dense cascade cores in which several secondaries contribute to the same pulse. In Figure 13, we show the zoomed-in hard tails of the simulated and experimental distributions in standard flux units. The tail endpoint reflects the rarest and most intense charged particle deposits produced by the most energetic secondaries in the atmospheric cascade. The experimental data tail ends at about 200 MeV. This endpoint aligns with the 10 GeV simulation, is higher than the 7.3 GeV case, and is clearly shorter than the 15 and 20 GeV simulations, which extend to approximately 230 and 250 MeV, respectively.

Thus, the defining feature of the hard tail—its extension—suggests a relatively soft, cutoff-limited primary population and does not support a significant contribution comparable to the 15 or 20 GeV monoenergetic templates. In Figure 14, we show the energy dependence of the number of muons reaching the detector as a function of primary proton energy. The figure confirms the trend shown in Figure 13, namely that higher-energy primaries yield many more muons at the observation level than lower-energy primaries.

6. Further Work

We present an analysis of recovered secondary energy spectra derived from energy-deposit histograms to estimate the most probable maximum energy of solar protons. In this analysis, we primarily use phenomenological parameters, such as the muon-to-neutron ratio, and visual comparisons of simulated and measured energy spectra. We recognize that the ultimate goal of GLE research is to directly recover the solar proton spectrum and determine its hardness. However, several challenges hinder this goal. Modern shower simulations face persistent issues with muons, known as the muon puzzle: observed showers contain more muons or exhibit a different muon distribution than predicted by standard hadronic models (Dembinski et al., 2022). For the CORSIKA chain, this

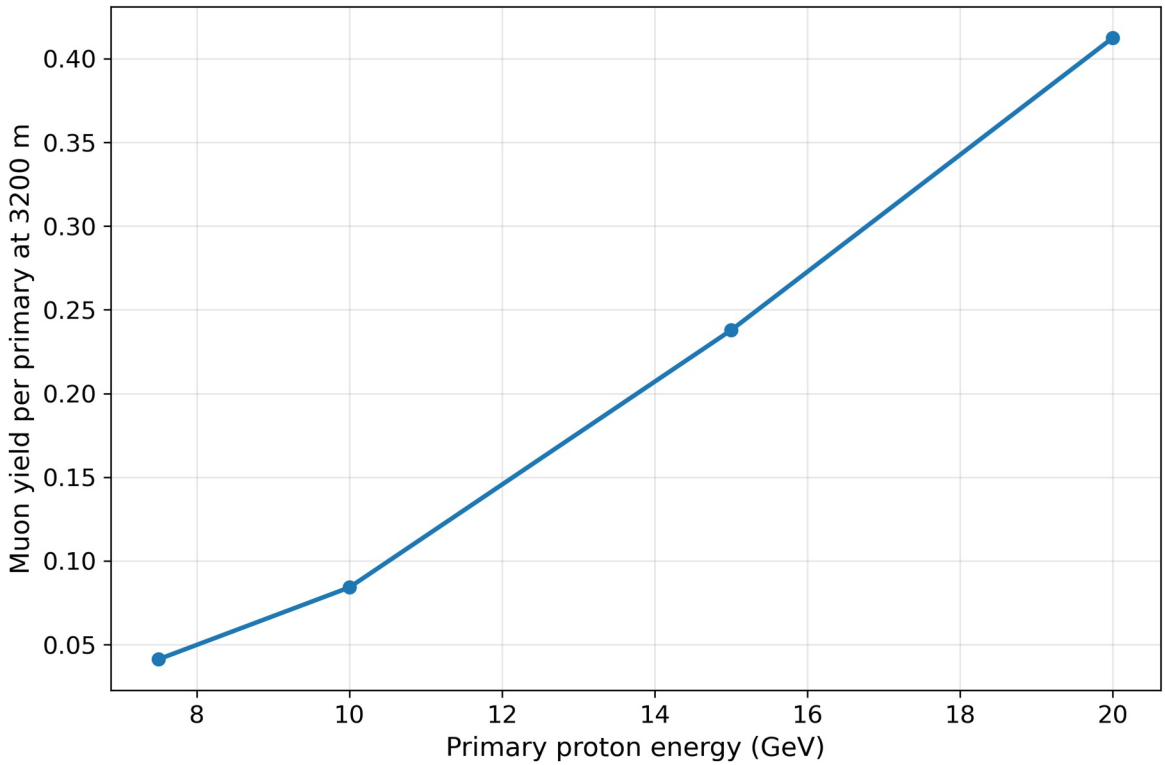

Figure 14. Simulated muon yield dependence on primary proton energy.

issue is even more critical because the sub-TeV region near the transition between QGSJETII-04 and URQMD is a regime where models differ significantly. A detailed comparison shows that QGSJETII-04, SIBYLL, EPOS, and UrQMD produce notably different ground-level muon and electromagnetic distributions (Pastor-Gutiérrez et al., 2021; Pyras et al., 2025); UrQMD, in particular, can spread muons over a wider area and cause an overall deficit of ground-level components under certain conditions, while QGSJETII-04 tends to concentrate muons near the core. We need to conduct a comparative analysis of models, and we have already begun discussions with model authors to tune the model parameters for the GeV region. Possibly, the neutron–muon spectrometric constraints on the GLE proton spectra will also help refine the strong interaction models. The simulation of the detector response should also be reconsidered to better align with the experimental event selection, and detector resolution must be constantly monitored. The results should be incorporated into the updated GEANT4 simulation of the detector response.

7. Conclusion

GLE 77, observed at Aragats on 11 November 2025, marks the first time that simultaneous neutron and muon energy spectra were obtained and analyzed together for this event using the combined capabilities of ASNT and SEVAN Light. It is also the first time that the effective upper energy of the solar-proton population has been constrained by local ground-based neutron–muon spectrometry rather than inferred solely from responses of the neutron monitor network. The reconstructed spectra, along with the energy dependence of the muon-to-neutron ratio, indicate that the event was dominated by solar protons near the local geomagnetic cutoff, with an effective upper energy around 9–10 GeV. Comparison with the unified CORSIKA + GEANT4 forward-modeling chain supports this interpretation, though current hadronic interaction models, including the QGSJETII-04/URQMD combination used here, still have known limitations in reproducing the muon content and lateral structure of atmospheric cascades. Despite these limitations, the combined neutron–muon diagnostics yield a clear physical result: GLE 77 was a relatively soft, cutoff-limited event without a significant proton component above 10 GeV.

This conclusion becomes especially clear when compared with GLE 69 of 20 January 2005. Earlier Aragats measurements of that event, based on high-energy muon observations, indicated a much harder solar-proton

spectrum extending beyond 20 GeV. The comparison shows that Aragats' observations are sensitive to spectral hardness and the effective upper energy of the solar proton population. Thus, this work extends previous Aragats studies from detecting hard GLE signatures to quantitatively distinguishing between near-cutoff and genuinely high-energy events. This capability is crucial for solar physics, as it provides insights into particle acceleration efficiency, and for space weather, offering a practical way to identify SEP events capable of generating a bulk of hazardous >50–100 MeV proton fluxes in near-Earth space in near-real time.

Beyond simply interpreting GLE 77 itself, this finding also has significance at the network level. SEVAN network hybrid detectors (Chilingarian, Karapetyan, Sargsyan, Asatryan et al., 2024; Chilingarian, Sargsyan et al., 2024) span the highest summit in Eastern Europe and Germany and measure the neutral and charged components of the CR flux, as well as >200 MeV muons. SEVAN Light enhances the capabilities of the SEVAN network from just monitoring counting rates to locally distinguishing between neutron- and muon-dominated secondary particles. The planned upgrades to network detectors will enable spectrometric measurements. Specifically, combining better detector-response calibration, unified minute-scale histogram processing, and applying the same reconstruction process across multiple stations will enable systematic comparisons of GLE hardness at different cutoff rigidities and altitudes. These improvements would enable the SEVAN network to operate as a distributed spectrometric system capable of constraining the high-energy limits of SEP events across diverse observational conditions.

Conflict of Interest

The authors declare no conflicts of interest relevant to this study.

Availability Statement

The full set of neutron and muon time series from the ASNT and the SEVAN Light detectors on GLE 69 and 77 is available in both numerical and graphical formats at the cosmic ray division's database of the Yerevan Physics Institute: http://crd.yerphi.am/adei/. The WIKI section of the database contains instructions on selecting appropriate detectors and times, as well as on uploading data.

GOES proton data shown in Figure 4 are publicly available at https://www.swpc.noaa.gov/products/goes-proton-flux.

The neutron monitor data shown in Figure 5 are publicly available at https://www.nmdb.eu.

Acknowledgments
The authors acknowledge the support of the Science Committee of the Republic of Armenia (Research Project No. 21AG-1C012). We also thank the NMDB database, established under the European Union's FP7 program (contract no. 213007), for providing access to neutron monitor data.

References

Agarwal, R., Mishra, R. K., & Mishra, D. (2026). Recent solar events and high-energy cosmic ray particles. *International Journal of Science, Engineering and Technology*, *14*(2), 1–15.

Agostinelli, S., Allison, J., Amako, K., Apostolakis, J., Araujo, H., Arce, P., et al. (2003). GEANT4 - A simulation toolkit. *Nuclear Instruments & Methods in Physics Research, Section A*, *506*(3), 250–303. https://doi.org/10.1016/S0168-9002(03)01368-8

Asvestari, E., Willamo, T., Gil, A., Usoskin, I., Kovaltsov, G., Mikhailov, V., & Mayorov, A. (2017). Analysis of ground-level enhancements (GLE): Extreme solar energetic particle events have hard spectra. *Advances in Space Research*, *60*(4), 781–787. https://doi.org/10.1016/j.asr.2016.08.043

Balabin, Y., Gvozdevsiy, B. B., & Germanrno, A. V. (2026). GLE77 Event of November 11, 2025. *Geomagnetism and Aeronomy*, *66*, 499–514. https://doi.org/10.7868/S3034502226030038

Bostanjan, N., Chilingarian, A., Eganov, V., & Karapetyan, G. (2007). On the production of highest-energy solar protons on 20 January 2005. *Advances in Space Research*, *39*(9), 1454–1457. https://doi.org/10.1016/j.asr.2007.03.024

Butikofer, R., & Fluckiger, E. O. (2015). What are the causes for the spread of GLE parameters deduced from NM data? *Journal of Physics: Conference Series*, *632*(1), 012053. https://doi.org/10.1088/1742-6596/632/1/012053

Chilingarian, A. (2009). Statistical study of the detection of solar protons of highest energies on 20 January 2005. *Advances in Space Research*, *43*(4), 702–707. https://doi.org/10.1016/j.asr.2008.10.005

Chilingarian, A., Chilingaryan, S., & Hovsepyan, G. (2015). Calibration of particle detectors for secondary cosmic rays using gamma-ray beams from thunderclouds. *Astroparticle Physics*, *69*, 37–43. https://doi.org/10.1016/j.astropartphys.2015.03.011

Chilingarian, A., Daryan, A., Arakelyan, K., Hovhannisyan, A., Mailyan, B., Melkumyan, L., et al. (2010). Ground-based observations of thunderstorm-correlated fluxes of high-energy electrons, gamma rays, and neutrons. *Physical Review D*, *82*(4), 043009. https://doi.org/10.1103/PhysRevD.82.043009

Chilingarian, A., Hovsepyan, G., Arakelyan, K., Chilingaryan, S., Danielyan, V., Avakyan, K., et al. (2009). Space environmental viewing and analysis network (SEVAN). *Earth, Moon, and Planets*, *104*(1–4), 195–204. https://doi.org/10.1007/s11038-008-9288-1

Chilingarian, A., Hovsepyan, G., Aslanyan, D., Karapetyan, T., Sargsyan, B., & Svechnikova, E. (2023). Thunderstorm ground enhancements observed on Aragats Mountain in Armenia in the wintertime. *EPL*, *143*(5), 59002. https://doi.org/10.1209/0295-5075/acf340

Chilingarian, A., Hovsepyan, G., & Hovhannisyan, A. (2011). Particle bursts from thunderclouds: Natural particle accelerators above our heads. *Physical Review D*, *83*(6), 062001. https://doi.org/10.1103/PhysRevD.83.062001

Chilingarian, A., Hovsepyan, G., Karapetyan, T., Aslanyan, D., Chilingaryan, S., & Sargsyan, B. (2023). Genesis of thunderstorm ground enhancements. *Physical Review D*, *107*(10), 102003. https://doi.org/10.1103/PhysRevD.107.102003

Chilingarian, A., Hovsepyan, G., Karapetyan, T., Khanykyanc, Y., Pokhsraryan, D., Sargsyan, B., et al. (2022). Multi-messenger observations of thunderstorm-related bursts of cosmic rays. *Journal of Instrumentation*, *17*(7), P07022. https://doi.org/10.1088/1748-0221/17/07/P07022

Chilingarian, A., Hovsepyan, G., Karapetyan, T., Kozliner, L., Chilingaryan, S., Pokhsraryan, D., & Sargsyan, B. (2022). The horizontal profile of the atmospheric electric fields as measured during thunderstorms by the network of NaI spectrometers located on the slopes of mt. Aragats. *Journal of Instrumentation*, *17*(10), P10011. https://doi.org/10.1088/1748-0221/17/10/P10011

Chilingarian, A., Hovsepyan, G., Karapetyan, T., Sargsyan, B., & Chilingaryan, S. (2022). Measurements of energy spectra of relativistic electrons and gamma-rays from avalanches developed in the thunderous atmosphere with Aragats Solar Neutron Telescope. *Journal of Instrumentation*, *17*(3), P03002. https://doi.org/10.1088/1748-0221/17/03/P03002

Chilingarian, A., Karapetyan, T., Sargsyan, B., Asatryan, K., & Gabaryan, G. (2024). Influence of magnetosphere disturbances on particle fluxes measured by ground-based detector. *EPL*, *148*(1), 19001. https://doi.org/10.1209/0295-5075/ad7e4c

Chilingarian, A., Karapetyan, T., Sargsyan, B., Knapp, J., Walter, M., & Rehm, T. (2024a). Energy spectra of the first TGE observed on Zugspitze by the SEVAN Light detector compared with the energetic TGE observed on Aragats. *Astroparticle Physics*, *156*, 102924. https://doi.org/10.1016/j.astropartphys.2024.102924

Chilingarian, A., Karapetyan, T., Sargsyan, B., Knapp, J., Walter, M., & Rehm, T. (2024b). Increase in the count rates of ground-based cosmic-ray detectors caused by the heliomagnetic disturbance on 5 November 2023. *EPL*, *146*(2), 24001. https://doi.org/10.1209/0295-5075/ad329c

Chilingarian, A., Melkumyan, L., Hovsepyan, G., & Reymers, A. (2007). The response function of the Aragats Solar Neutron Telescope. *Nuclear Instruments & Methods in Physics Research, Section A*, *574*(2), 255–263. https://doi.org/10.1016/j.nima.2007.02.097

Chilingarian, A., & Reymers, A. (2008). Investigations of the response of hybrid particle detectors for the Space Environmental Viewing and Analysis Network (SEVAN). *Annales Geophysicae*, *26*(2), 249–257. https://doi.org/10.5194/angeo-26-249-2008

Chilingarian, A., Sargsyan, B., Karapetyan, T., Aslanyan, D., Chilingaryan, S., Kozliner, L., & Khanikyanc, Y. (2024). Extreme electron and gamma-ray bursts registered on Aragats in 2023. *Physical Review D*, *110*(6), 063043. https://doi.org/10.1103/PhysRevD.110.063043

Clem, J. M., & Dorman, L. I. (2000). Neutron monitor response functions. *Space Science Reviews*, *93*(1–2), 335–359. https://doi.org/10.1023/A:1026508915269

Dembinski, H. P., Albrecht, J., Cazon, L., Fedynitch, A., Kampert, K. H., Pierog, T., et al. (2022). The Muon Puzzle in cosmic-ray induced air showers and its connection to the Large Hadron Collider. *Astrophysics and Space Science*, *367*(3), 25. https://doi.org/10.1007/s10509-022-04054-5

Dorman, L. I. (2004). Cosmic rays in the Earth's atmosphere and underground. Kluwer Academic Publishers. https://doi.org/10.1007/978-1-4020-2113-8

Gopalswamy, N., Xie, H., Yashiro, S., Akiyama, S., Mäkelä, P., & Usoskin, I. G. (2012). Properties of ground-level enhancement events and associated solar eruptions during solar cycle 23. *Space Science Reviews*, *171*(1–4), 23–60. https://doi.org/10.1007/s11214-012-9890-4

Grieder, P. K. F. (2001). *Cosmic rays at Earth*. Elsevier.

Heck, D., Knapp, J., Capdevielle, J. N., Schatz, G., & Thouw, T. (1998). CORSIKA: A Monte Carlo code to simulate extensive air showers. Report FZKA-6019. Forschungszentrum Karlsruhe. https://doi.org/10.5445/IR/270043064

Jarry, M., Palmroos, C., Lavasa, E., Talebpour Sheshvan, N., Koeberle, M., Heber, B., et al. (2026). Catalogue and statistics of >100 MeV solar proton events during solar cycles 23-25 from SOHO/ERNE observations. *Astronomy and Astrophysics*. in press. https://doi.org/10.48550/arXiv.2603.10903

Kress, B. T., Rodriguez, J. V., & Onsager, T. G. (2020). The GOES-R Space Environment In Situ Suite (SEISS): Measurement of energetic particles in geospace. In S. J. Goodman, T. J. Schmit, J. Daniels, & R. J. Redmon (Eds.), *The GOES-R series* (pp. 243–250). Elsevier. https://doi.org/10.1016/B978-0-12-814327-8.00020-2

Mishev, A. L., Heber, B., Klein, K.-L., Vainio, R., Mavromichalaki, H., Raukunen, O., et al. (2026). Ground Level Enhancement GLE #77 on 11 November 2025: A data summary. *Advances in Space Research*, *77*(9), 9764–9783. https://doi.org/10.1016/j.asr.2026.03.023

Mishev, A. L., & Usoskin, I. G. (2016). Analysis of the ground level enhancements on 14 July 2000 and on 13 December 2006 using neutron monitor data. *Solar Physics*, *291*(4), 1225–1239. https://doi.org/10.1007/s11207-016-0877-2

Mishev, A. L., & Usoskin, I. G. (2020). Current status and possible extension of the global neutron monitor network. *Journal of Space Weather and Space Climate*, *10*, 17. https://doi.org/10.1051/swsc/2020020

Muraki, Y., Tsuchiya, H., Fujiki, K., Masuda, S., Matsubara, Y., Menjyo, H., et al. (2007). A solar neutron telescope in Tibet and its capability examined by the 1998 November 28th event. *Astroparticle Physics*, *28*(1), 119–131. https://doi.org/10.1016/j.astropartphys.2007.04.012

Ostapchenko, S. (2024). QGSJET-III model of high energy hadronic interactions: The formalism. *Phys.Rev.D*, *109*(3), 034002. https://doi.org/10.1103/PhysRevD.109.034002

Pastor-Gutiérrez, Á., Schoorlemmer, H., Parsons, R. D., & Schmelling, M. (2021). Sub-TeV hadronic interaction model differences and their impact on air showers. *The European Physical Journal C*, *81*, 269. https://doi.org/10.1140/epjc/s10052-021-09160-2

Pyras, L., Soldin, D., & Riehn, F. (2025). Probing hadronic interactions with high-energy and low-energy muons in extensive air showers. *Proceedings of Science*, 368. https://doi.org/10.22323/1.501.0368

Reames, D. V. (2013). The two classes of solar energetic particles. *Space Science Reviews*, *175*(1–4), 53–92. https://doi.org/10.1007/s11214-013-9958-9

Reames, D. V. (2021). Solar energetic particles: A modern primer on understanding sources, acceleration and propagation. In *Lecture notes in physics* (2nd ed., Vol. 978). Springer. https://doi.org/10.1007/978-3-030-66402-2

Sato, T. (2016). Analytical model for estimating the zenith angle dependence of terrestrial cosmic-ray fluxes. *PLoS One*, *11*(8), e0160390. https://doi.org/10.1371/journal.pone.0160390

Shea, M. A., & Smart, D. F. (2012). Space weather and the ground-level solar proton events of the 23rd solar cycle. *Space Science Reviews*, *171*(1–4), 161–188. https://doi.org/10.1007/s11214-012-9923-z

Tylka, A. J., & Dietrich, W. F. (2009). A new and comprehensive analysis of proton spectra in ground-level enhanced (GLE) solar particle events. In *Proceedings of the 31st international cosmic ray conference, lodz* (Vol. SH3).

Zazyan, M., & Chilingarian, A. (2009). Calculations of the sensitivity of the particle detectors of ASEC and SEVAN networks to galactic and solar cosmic rays. *Astroparticle Physics*, *32*(3–4), 185–192. https://doi.org/10.1016/j.astropartphys.2009.08.001